Nanoscale

Accepted Manuscript

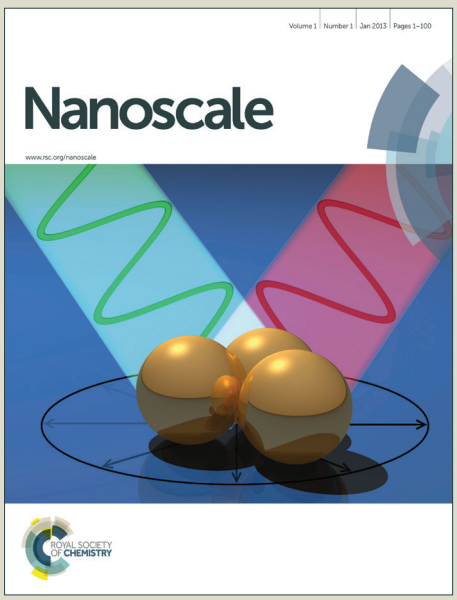

ROYAL SOCIETY OF CHEMISTRY

www.rsc.org/nanoscale

ARTICLE TYPE www. rsc.org/xxxxxx | XXXXXXXX

Dirac point movement and topological phase transition in patterned graphene†

Marc Dvorak[a] **and Zhigang Wu***[a]

Received Xth XXXXXXXXXX 20XX, Accepted Xth XXXXXXXXX 20XX
First published on the web Xth XXXXXXXXXX 200X
DOI: 10.1039/b000000x

The honeycomb lattice of graphene is characterized by linear dispersion and pseudospin chirality of fermions on the Dirac cones. If lattice anisotropy is introduced, the Dirac cones stay intact but move in reciprocal space. Dirac point movement can lead to a topological transition from semimetal to semiconductor when two inequivalent Dirac points merge, an idea that has attracted significant research interest. However, such movement normally requires unrealistically high lattice anisotropy. Here we show that anisotropic defects can break the C_3 symmetry of graphene, leading to Dirac point drift in the Brillouin zone. Additionally, the long-range order in periodically patterned graphene can induce intervalley scattering between two inequivalent Dirac points, resulting in a semimetal-to-insulator topological phase transition. The magnitude and direction of Dirac point drift are predicted analytically, which are consistent with our first-principles electronic structure calculations. Thus, periodically patterned graphene can be used to study the fascinating physics associated with Dirac point movement and the corresponding phase transition.

Since the isolation of graphene, a two-dimensional (2D) honeycomb lattice of carbon (C) atoms, tremendous research efforts have been spent on the physics of the honeycomb lattice and Dirac points[1–3]. Dirac points manifest themselves in many intriguing phenomena, including massless fermions in graphene[3] and conducting surface states in topological insulators[4]. Dirac points can appear in any 2D lattice if parameters are appropriately adjusted, but the honeycomb lattice is the simplest and most natural realization. Graphene is a tangible, solid-state example of such a lattice with C_3 symmetry, but Dirac points also exist on honeycomb lattices without C_3 symmetry. One possible realization is strained graphene[5–7], but most experiments focus on anisotropy in honeycomb optical lattices[8–12], which can be precisely tuned to study massless Dirac fermions and their correlated phases.

In pristine graphene, the Dirac points ($\mathbf{D}$ and $\mathbf{D}' = -\mathbf{D}$) are located at the corners of the hexagonal Brillouin zone ($\mathbf{K}$ and $\mathbf{K}' = -\mathbf{K}$). When lattice anisotropy is introduced, the Dirac points move away from these positions. If the anisotropy is large enough, the Dirac points will eventually merge and a topological transition occurs.[13–15] The significance of this transition in condensed-matter physics has lead to extensive theoretical and experimental efforts[8,10,12–14]. However, this phenomenon is extremely challenging to observe in graphene or any other solid-state materials because of the unrealistic lattice anisotropy required. Instead, researchers mainly focus on artificial honeycomb lattices, including trapping ultracold atoms in honeycomb optical lattices[8,13] and nano-patterning 2D electron gases[16,17] for better tunability.

In this article, we present a new mechanism to move Dirac points and facilitate a topological transition in graphene based on periodic patterning of defects. Specifically, anisotropic defects cause the Dirac points to shift, the magnitude of which can be evaluated according to the renormalization of graphene's three hopping parameters. Furthermore, the long-range order introduced by periodic defects can induce intervalley scattering between two Dirac points. The intervalley scattering condition leads to a transition from semimetal to semiconductor without requiring the Dirac points to merge and annihilate. Our prior work[18,19] has focused exclusively on scattering induced by idealized defects that have C_3 symmetry themselves. Here, we consider complex, anisotropic defect structures and focus on the effects of both local defect geometry and long-range order. Our theoretical analysis is consistent with *ab-initio* electronic structure calculations. Therefore, patterned graphene can serve as a tunable platform to adjust the effective mass of fermions and study electronically correlated topological phase transitions.

1 Results

1.1 Quantifying anisotropy in patterned graphene

Various periodic defects have been realized on graphene, such as partially H-passivated graphene[20,21], graphene

† Electronic Supplementary Information (ESI) available: [details of any supplementary information available should be included here]. See DOI: 10.1039/b000000x/

[a] *Department of Physics, Colorado School of Mines, Golden, CO, USA. E-mail: zhiwu@mines.edu*

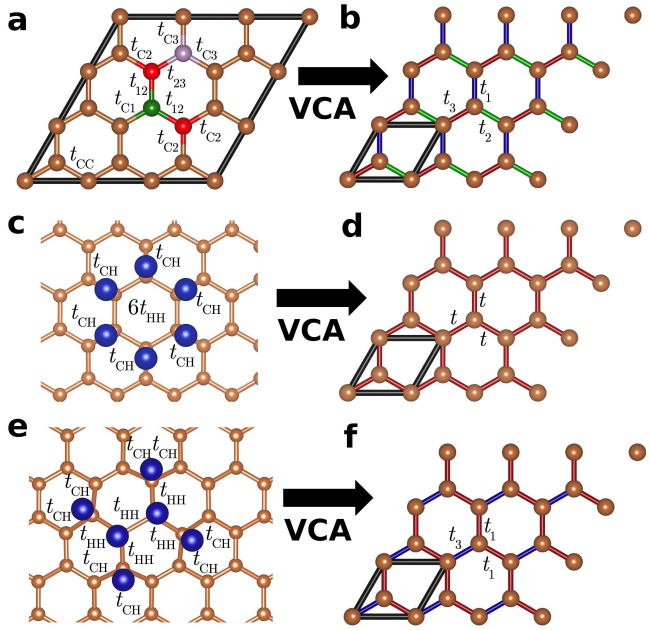

Fig. 1 The virtual crystal approximation. a, b, In the VCA, a defected graphene supercell is replaced by a 2-atom primitive cell with supercell averaged hopping parameters t_1, t_2 and t_3. **c, d**, Isotropic defect of a 6C-ring passivated with hydrogen that preserves the local C_3 symmetry so that $t_1 = t_2 = t_3 = t$. **e, f**, Anisotropic H-passivation defect formed from adjacent halves of two 6C-rings (split-6C) that breaks C_3 symmetry with $t_1 = t_2 \neq t_3$.

nanomesh[22,23] (GNM), and graphene doped with patches of hexagonal BN[24]. Recent works[22,23] have demonstrated functional field-effect transistors based on patterned semiconducting graphene; however, the interplay between local defect configurations and long-range order in these materials is still unclear.

We have studied isotropic defects without breaking the local C_3 symmetry in the past[18,19,25], i.e., on average, the three hopping parameters (t) in the tight-binding (TB) graphene model[3,26] remain identical. Here we focus on *anisotropic* defects that result in different renormalized hopping strengths. The anisotropy in defected graphene can be quantified by simply averaging the three nearest-neighbor hopping parameters in a supercell, i.e., the virtual crystal approximation (VCA)[27,28] in solid-state physics. Based on the VCA, we model a large defected graphene supercell by a two-atom primitive cell with three distinct hopping parameters t_1, t_2, and t_3, as illustrated in Figure 1. The details of our VCA model are in Supplementary Information.

1.2 Dirac point drift

While the defected supercells shown on the left side of Figure 1 are difficult to deal with, their corresponding VCA model structures on the right side are well understood analytically at the TB level of theory[5,13–15]. In a honeycomb lattice with three different hopping parameters and bond length a, Dirac points still satisfy $\mathbf{D}' = -\mathbf{D}$, but their locations[13] are:

$$\begin{aligned} D_{x,\pm} &= \pm\frac{2}{a}\arccos\left(-\sqrt{\frac{t_3^2-(t_2-t_1)^2}{4t_1t_2}}\right), \\ D_{y,\pm} &= \pm\frac{2}{\sqrt{3}a}\mathrm{sgn}(t_1-t_2) \\ &\quad \arccos\left(\frac{t_1+t_2}{t_3}\sqrt{\frac{t_3^2-(t_2-t_1)^2}{4t_1t_2}}\right). \end{aligned} \tag{1}$$

Previous work[5] has demonstrated that strain can move Dirac points according to Eq. (1). Here, we show that we can modify the VCA hopping parameters and move the Dirac points along predictable paths in reciprocal space by adjusting the local defect structure, as demonstrated by Figure 2. Specifically, Figure 2b and Figure 2c indicate that Dirac points drift along the k_y axis for defects with $t_1 = t_2 \neq t_3$, corresponding to the case sketched in Figure 1f. Figure 2d and Figure 2e show the movement of Dirac points when all three VCA hopping parameters are unequal, $t_1 \neq t_2 \neq t_3$, corresponding to Figure 1b. Since boron nitride doping produces a much weaker perturbation than hydrogen passivation, the Dirac point shift in Figure 2c and Figure 2e is smaller than that in Figure 2b and Figure 2d, respectively.

Using Eq. (1), one can determine the magnitude of Dirac point movement in patterned graphene in terms of the VCA hopping parameters. For instance, the anisotropic split-6C ring defect (Figure 1e) leads to:

$$\begin{aligned} t_1 &= t_2 = \left(1-\frac{4}{3}f_d\right)t_{\mathrm{CC}} + \frac{2}{3}f_d(t_{\mathrm{HC}}+t_{\mathrm{HH}}), \\ t_3 &= \left(1-\frac{5}{3}f_d\right)t_{\mathrm{CC}} + \frac{4}{3}f_d t_{\mathrm{HC}} + \frac{1}{3}f_d t_{\mathrm{HH}}, \end{aligned} \tag{2}$$

where the defected fraction $f_d \equiv N_{\mathrm{H}}/N_{\mathrm{C}}$, with N_{H} and N_{C} the numbers of H and C atoms in a supercell. t_{CC}, t_{HC}, and t_{HH} are hopping parameters between two C atoms without H passivation, one bare C atom and one passivated C atom, and two passivated C atoms, respectively. Inserting Eq. (2) into Eq. (1) and expanding the arccos function to linear order in the defect fraction f_d, we obtain the position of the shifted Dirac point $\mathbf{D}$ for graphene with 6C-split defects:

$$D_y^{\mathrm{split}} = \frac{4\pi}{3a} - \frac{2(t_{\mathrm{CC}}-2t_{\mathrm{HC}}+t_{\mathrm{HH}})f_d}{3\sqrt{3}at_{\mathrm{CC}}} + \mathscr{O}[f_d]^2. \tag{3}$$

Here a is the nearest-neighbor C-C bond length, and we orient our coordinate system so that the movement of Dirac points is

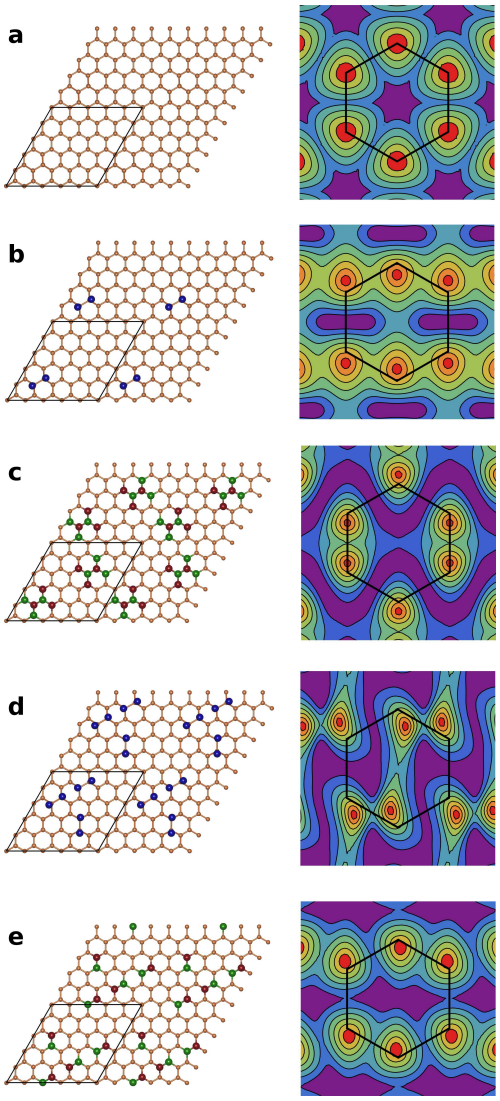

Fig. 2 Dirac point drift. Crystal structures (left column) and contour plots of the energy for the highest valence band (right column) at each **k**-point in the Brillouin zone (black hexagon, for the 5×5 supercell) of defected graphene. The highest energy points (centers of the red areas) indicate the location of Dirac points. **a**, Pristine graphene. **b** and **d**, Partial hydrogen passivation. **c** and **e**, Boron nitride (BN) doping. Here golden, blue, green, and dark red dots represent C, H, B and N atoms, respectively. All graphene structures have the same 5×5 hexagonal supercell indicated by solid black lines (left column).

along the k_y direction for the case of $t_1 = t_2 \neq t_3$ (Figure 2b and Figure 2c).

Another example is the 'pair' defect formed by two adsorbed H atoms on top of a pair of adjacent C atoms (Figure 2b). Depending on the defect fraction f_d, the Dirac point moves to

$$D_y^{\text{pair}} = \frac{4\pi}{3a} + \frac{2(t_{\text{CC}} - 2t_{\text{HC}} + t_{\text{HH}})f_d}{\sqrt{3}at_{\text{CC}}} + \mathcal{O}[f_d]^2. \quad (4)$$

Comparing the slopes of the linear expansions in Eqs. (3) and (4), we draw two conclusions: (i) split and pair defects cause the Dirac point to drift in opposite directions and (ii) for an identical defect fraction, the magnitude of the k_y drift for split defects is less than that of pair defects. Direct verification of Dirac point movement predicted by Eqs. (3) and (4) is difficult because the values of t_{HC} and t_{HH} are unknown. Instead, we perform first-principles electronic structure calculations to examine the above two conclusions drawn from Eqs. (3) and (4).

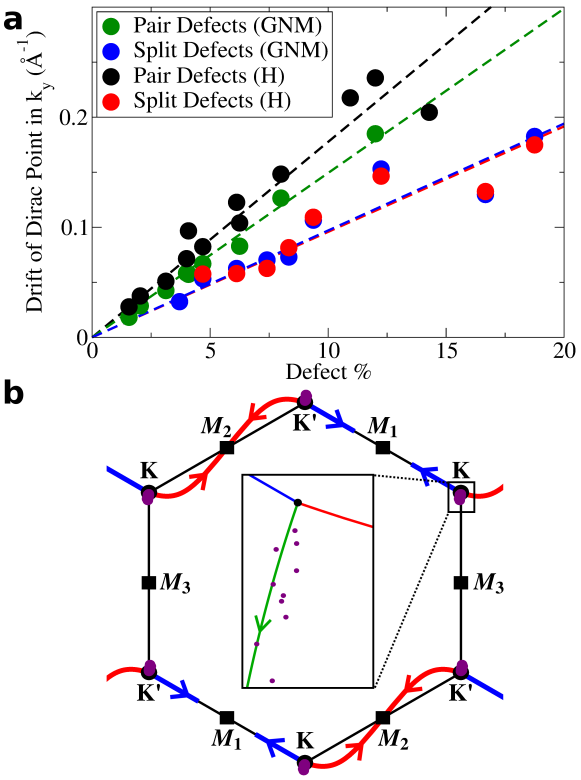

Fig. 3 Dirac point drift vs defect fraction. a, Magnitude of Dirac point drift in 4 types of defected graphene as functions of defect fraction f_d. Dashed lines are linearly fitted to calculated data plotted with solid dots. For split defects, the drift is along the $-k_y$ direction, while the drift is along $+k_y$ for pair defects. Results for BN doping are presented in Supplementary Information. **b**, Blue and red solid lines are trajectories of Dirac points in reciprocal space as f_d increases for the two examples discussed in text. Purple dots are numerical data for the defect shown in Figure 2e and the green line is a numerical fit.

We track the movement of Dirac points in the $\pm k_y$ direction

for graphene supercells with pair and split defects created by partial H-passivation, vacancies, and BN doping. We consider arbitrary supercell geometries and sizes to test the generality of our theory. By unfolding the Brillouin zones of these materials, we find the Dirac-like points derived from the Dirac points of pristine graphene. Our defining criterion for Dirac-like points is a gapless state with linear dispersion nearby. Some materials may have very small band gaps due to buckling of the graphene sheet or broken inversion symmetry. For our purposes, these materials are practically gapless. Not all materials show these Dirac-like points; the exceptions to this rule are semiconductors (when the topological phase transition occurs) and will be discussed shortly. Figure 3a demonstrates that for vacancy defects (GNM), the ratio of the fitted slopes for split and pair defects is 0.64, while this ratio is 0.54 for H-passivation. The direction of the Dirac point drift due to split defects is, as predicted, opposite that of pair defects (see Figure 2b and Figure 2c). Our VCA tight binding model, therefore, can qualitatively predict the movement of Dirac points in graphene with anistropic defects.

We now turn our attention to the case $t_1 \neq t_2 \neq t_3$. It proves convenient to reparameterize the VCA hopping parameters according to

$$\begin{aligned} t_1 &= (1-f_d)t_{CC} + f_d t_1', \\ t_2 &= (1-f_d)t_{CC} + f_d t_2', \\ t_3 &= (1-f_d)t_{CC} + f_d t_3'. \end{aligned} \quad (5)$$

Here, the t_i' parameters represent the hopping in the i-th direction averaged *only* for the defected C atoms. These values enter the VCA with the weight f_d, and the remainder of the supercell is the usual C-C hopping with the weight $(1-f_d)$. We explore the evolution of the Dirac points as a function of defect fraction f_d for different combinations of t_1', t_2' and t_3' analytically (details in Supplementary Info) and then compare with numerical results from first-principles calculations.

Three examples are plotted in Figure 3b. The blue curve corresponds to $t_1' = t_{2'}' = 6t_{CC}$, $t_3' = 11t_{CC}$, the red curve depicts the case $t_1' = 4t_{CC}$, $t_2' = 3t_{CC}$, $t_3' = -t_{CC}$, whereas the green curve is a numerical fit to the purple data points computed for the BN defect shown in Figure 2e. All these trajectories begin at the **K** or **K**′ points and evolve towards an **M** point of the Brillouin zone as f_d approaches 1. Note that the upper bound on anistropy is when f_d is 1, which may not induce high enough anisotropy to merge the Dirac points at an **M** point. If they do merge, a topological transition from semimetal to semiconductor occurs. Figure 3b suggests that, among these three cases, only the red curve can cause the Dirac points to merge. However, such large values of f_d and t_i' are unrealistic, and any practical anisotropy induced by defects can only generate a small amount of Dirac point drift (e.g., the green curve and purple data points). Nonetheless, the intriguing semimetal to semiconductor phase transition can be realized in periodically defected graphene by intervalley scattering.

1.3 Topological phase transition

While scientifically very interesting, drifting Dirac points also have important ramifications for technological applications. When the Dirac points drift on top of each other, a topological transition occurs and a bulk band gap opens.[5,9,13,14] As already stated, the degree of anisotropy required for the Dirac points to merge is unreasonably large. For example, in strained graphene, uniaxial strains of around 20% are necessary to facilitate this transition[6,7].

Fortunately, the long-range order created by defects provides an alternative route to opening a band gap at the Dirac points without the need for such high anisotropy[18,19,25,29,30]. Previous work has shown that band gap opening under an external potential is not possible when the potential varies slowly over the scale of the interatomic distance[31–34]. However, if the external potential $U(\mathbf{G})$ has appreciable contributions at high wave vectors $|\mathbf{G}| \sim |\mathbf{D}|$, as we expect in defected graphene, bulk band gap opening is possible. In this case, even though the Dirac points do not merge, the Dirac cones themselves and their associated $\pm\pi$ Berry phases no longer exist, indicating the topological character of the transition. An examination of the band topology in the presence of intervalley scattering in graphene will be presented in future work.

The topological phase transition takes place when the intervalley scattering condition $U(\mathbf{D}-\mathbf{D}') \neq 0$ is satisfied. This condition is equivalent to the requirement that the Dirac points drift onto a supercell reciprocal lattice vector (**G**) or onto a middle point $\mathbf{M} = \mathbf{G}/2$. To test our prediction, we numerically search for defected graphene structures with drifted Dirac points that satisfy the intervalley scattering condition. This search is quite challenging because the degree of Dirac point movement is only known numerically, and each supercell has its own set of reciprocal lattice vectors. For a given defect, changing the size of the supercell changes not only f_d and the position of the Dirac points, but also changes the high symmetry points of the Brillouin zone.

Figure 4a shows a successful search for such a transition schematically. For a fixed defect of three H-passivation pairs, the drift of the Dirac point decreases as the size of supercell increases from 5×5 to 8×8 (red to green, Figure 4b to Figure 4d). As f_d decreases, the shift of Dirac points is reduced; the 7×7 supercell has an **M** point overlapping with **D**, as indicated in Figure 4a, inducing intervalley scattering between two Dirac points and resulting in gapped and parabolic dispersion at $\mathbf{M}_3$ in the calculated electronic band structure.

One can also add defects to a fixed supercell to increase defect fraction f_d and Dirac point drift, as summarized in Figure 5. Figure 5a, Figure 5c, and Figure 5e show that the Dirac point drifts away from $\mathbf{A}_2$ and towards a reciprocal lattice vec-

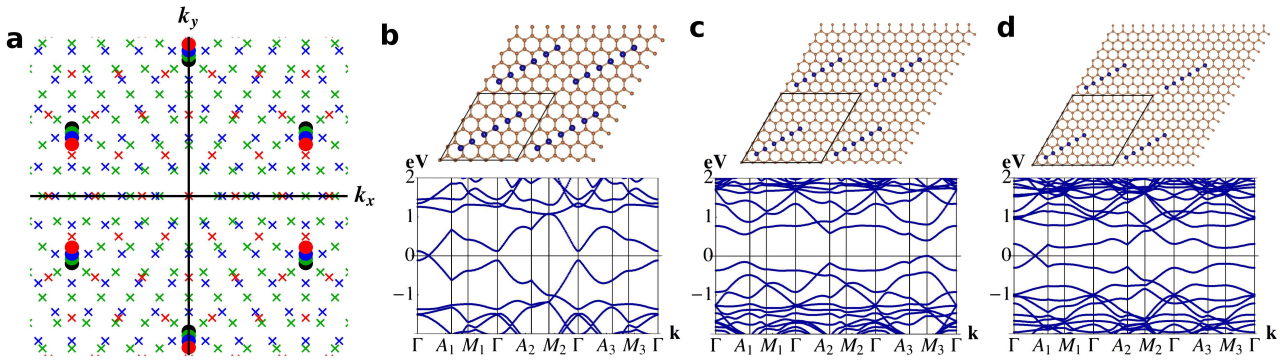

Fig. 4 Numerical search for topological phase transition in graphene with anisotropic defects. a, Black dots indicate the original positions of the Dirac points in pristine graphene. After unfolding their respective Brillouin zones, red and green dots correspond to equivalent positions of the Dirac point for 5×5 (panel **b**) and 8×8 (panel **c**) supercells subject to three H-pair defects. The blue dot corresponds to the unfolded **k**-point location of the band gap in a 7×7 supercell (panel **c**) subject to three H-pair defects. Red, blue, and green $\times$'s mark the reciprocal lattice vectors of their respective structures. Only the blue dot falls at an **M** or **G** point of its Brillouin zone. **b**, **c** and **d**, Crystal and electronic structures of the 5×5, 7×7 and 8×8 supercells with three H-pair defects presented in panel **a**.

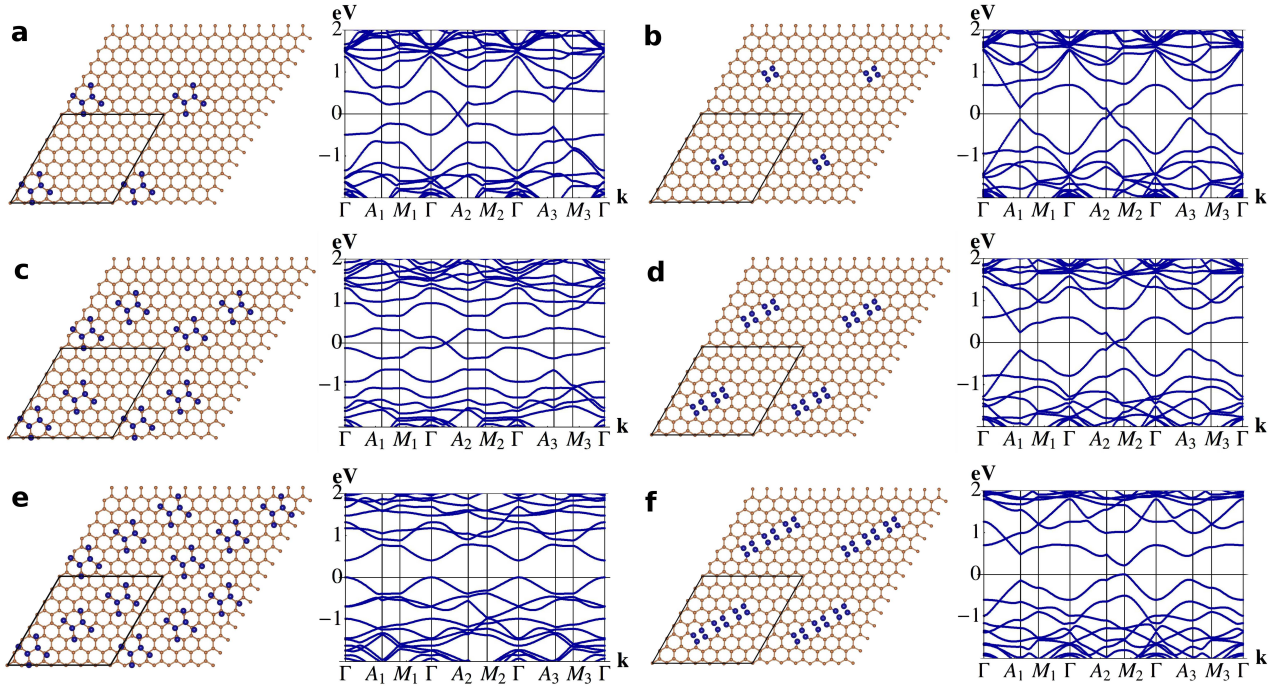

Fig. 5 Topological phase transition in graphene by changing number of defects in a supercell. a, **c** and **e** Crystal (left) and electronic (right) structures of a 7×7 graphene supercell subject to one, two, and three split H-passivation defects, respectively. **b**, **d** and **f**, Crystal (left) and electronic (right) structures of a 7×7 graphene supercell subject to one, two, and three pair vacancy defects, respectively.

tor **G** as f_d increases. Once the Dirac point drifts onto a **G** vector, a topological phase transition occurs and the resulting electronic band structure has a gap at the Γ-point. Figure 5b, Figure 5d and Figure 5f show a similar trend: their Dirac points move towards an **M**-point. Once the Dirac point drifts onto $\mathbf{M}_2$, the intervalley scattering condition is satisfied and a band gap opens at $\mathbf{M}_2$.

2 Discussion

We have demonstrated the sensitivity of a defected graphene sheet's electronic structure to the geometries of both the supercell and the defect structure. The movement of Dirac points is well predicted by considering the local configuration of defects and the supercell size. The appearance of a band gap depends on both the local defect structure and the long range order. Therefore, patterned graphene could be a practical material to investigate the fundamental physics of Dirac point movement and the relevant topological phase transition in a solid-state system.

The seemingly complicated behaviors of Dirac points in these complex graphene systems can be understood by a simple effective TB model based on the VCA. Because the defect structures vary on the scale of the interatomic distance, they can induce intervalley scattering between the Dirac points and cause a semimetal-to-semiconductor transition. Not surprisingly, the intervalley scattering mechanism has a strong resemblance to the annihilation of merging Dirac points, leading to a topological phase transition in both cases. However, overlap of Dirac points in the *supercell* Brillouin zone simply due to zone folding does *not* cause them to merge. For example, it is possible to construct a non-Bravais lattice of defected graphene such that the phase factors for each defect cancel, effectively reversing the appearance of a band gap and causing a semiconductor-to-semimetal transition[19]. In this case, the two Dirac points both overlap with $\mathbf{G}$ but they do *not* annihilate each other. The cancellation of phase factors is strong evidence that a scattering mechanism is responsible for band gap opening in patterned graphene, not the merging of Dirac points. We are preparing research for a future publication that details the character of the transition and band topology in the case of scattering off an external potential.

Finally, the technological importance of such semiconducting graphene structures cannot be understated. Patterned graphene sheets with sizable band gaps have already been fabricated as electronic devices[20–22,24,35]. Despite these successes, however, a fundamental understanding of defects on graphene was missing, especially regarding the interplay between long-range order and local defect configuration. Our theory points out that the long-range order offers possible intervalley scattering while the local defect configuration can move Dirac points. When Dirac points meet a supercell reciprocal lattice vector $\mathbf{G}$ or a middle point $\mathbf{M} = \mathbf{G}/2$, a topological phase transition occurs and the massless fermions gain effective mass. Therefore, our work not only provides a platform to investigate the fundamental physics of Dirac cones, but also presents a reliable road map to designing semiconducting graphene materials.

3 Methods

Our first-principles electronic structure calculations based on density functional theory were performed using the SIESTA package[36] using a triple-ζ polarized atomic basis set for carbon atoms, whose numerical accuracy has been rigorously tested against the planewave-based VASP program[37]. The 2D Brillouin zones of supercells were sampled on a 2×2 Monkhorst-Pack $\mathbf{k}$-point grid with good convergence due to very large unit cells. The generalized gradient approximation[38] was used for the exchange-correlation functional. All calculations are spin-polarized. Structures are optimized until the maximum atomic force is less than 0.02 eV/Å. Dangling bonds in GNM structures are passivated with hydrogen atoms.

Acknowledgements
This work was financially supported by DOE Early Career Award (No. DE-SC0006433). Computations were carried out at the Golden Energy Computing Organization at CSM and NERSC.

Correspondence
Correspondence and requests for materials should be addressed to Z.W. (email: zhiwu@mines.edu).

Additional Information
Supplementary Information accompanies this paper.

Competing financial interests: The authors declare no competing financial interests.

References

1 Novoselov, K. S.; Geim, A. K.; Morozov, S. V.; Jiang, D.; Zhang, Y.; Dubonos, S. V.; Grigorieva, I. V.; Firsov, A. A. *Science* **2004**, *306*, 666–669.
2 Geim, A. K.; Novoselov, K. S. *Nature Mater.* **2007**, *6*, 183–191.
3 Castro Neto, A. H.; Guinea, F.; Peres, N. M. R.; Novoselov, K. S.; Geim, A. K. *Rev. Mod. Phys.* **2009**, *81*, 109–162.
4 Hasan, M. Z.; Kane, C. L. *Rev. Mod. Phys.* **2010**, *82*, 3045–3067.
5 Pereira, V. M.; Castro Neto, A. H.; Peres, N. M. R. *Phys. Rev. B* **2009**, *80*, 045401.
6 Ni, Z. H.; Yu, T.; Lu, Y. H.; Wang, Y. Y.; Feng, Y. P.; Shen, Z. X. *ACS Nano* **2008**, *2*, 2301–2305.
7 Farjam, M.; Rafii-Tabar, H. *Physica E* **2010**, *42*, 2109 – 2114.
8 Tarruell, L.; Greif, D.; Uehlinger, T.; Jotzu, G.; Esslinger, T. *Nature* **2012**, *483*, 302–305.

9 Ibañez Azpiroz, J.; Eiguren, A.; Bergara, A.; Pettini, G.; Modugno, M. *Phys. Rev. A* **2013**, *88*, 033631.

10 Zhu, S.-L.; Wang, B.; Duan, L.-M. *Phys. Rev. Lett.* **2007**, *98*, 260402.

11 Wang, L.; Fu, L. *Phys. Rev. A* **2013**, *87*, 053612.

12 Polini, M.; Guinea, F.; Lewenstein, M.; Manoharan, H. C.; Pellegrini, V. *Nature Nanotech.* **2013**, *8*, 625.

13 Wunsch, B.; Guinea, F.; Sols, F. *New J. Phys.* **2008**, *10*, 103027.

14 Montambaux, G.; Piéchon, F.; Fuchs, J.-N.; Goerbig, M. O. *Phys. Rev. B* **2009**, *80*, 153412.

15 Hasegawa, Y.; Kishigi, K. *Phys. Rev. B* **2012**, *86*, 165430.

16 Park, C. H.; Louie, S. G. *Nano Lett.* **2009**, *9*, 1793–1797.

17 Singha, A.; Gibertini, M.; Karmakar, B.; Yuan, S.; Polini, M.; Vignale, G.; Katsnelson, M. I. .; Pinczuk, A.; Pfeiffer, L. N.; West, K. W.; Pellegrini, V. *Science* **2011**, *332*, 1176–1179.

18 Dvorak, M.; Oswald, W.; Wu, Z. *Sci. Rep.* **2013**, *3*, 2289.

19 Dvorak, M.; Wu, Z. *Phys. Rev. B* **2014**, *90*, 115415.

20 Sessi, P.; Guest, J. R.; Bode, M.; Guisinger, N. P. *Nano Lett.* **2009**, *9*, 4343–4347.

21 Balog, R. et al. *Nature Mater.* **2010**, *9*, 315–319.

22 Bai, J.; Zhong, X.; Jiang, S.; Huang, Y.; Duan, X. *Nature Nanotech.* **2010**, *5*, 190–194.

23 Kim, M.; Safron, N. S.; Han, E.; Arnold, M. S.; Gopalan, P. *Nano Lett.* **2010**, *10*, 1125–1131.

24 Ci, L.; Song, L.; Jin, C.; Jariwala, D.; Wu, D.; Li, Y.; Srivastava, A.; Wang, Z. F.; Storr, K.; Balicas, L.; Liu, F.; Ajayan, P. M. *Nature Mater.* **2010**, *9*, 430–435.

25 Oswald, W.; Wu, Z. *Phys. Rev. B* **2012**, *85*, 115431.

26 Wallace, P. R. *Phys. Rev.* **1947**, *71*, 622–634.

27 Nordheim, L. *Ann. Physik* **1931**, *9*, 607 and 641.

28 Parmenter, R. H. *Phys. Rev.* **1955**, *97*, 587–598.

29 Ouyang, F.; Peng, S.; Yang, Z.; Chen, Y.; Zou, H.; Xiong, X. *Phys. Chem. Chem. Phys.* **2014**, *16*, 20524–20531.

30 Liu, X.; Zhang, Z.; Guo, W. *Small* **2013**, *9*, 1405–1410.

31 Park, C.-H.; Yang, L.; Son, Y.-W.; Cohen, M. L.; Louie, S. G. *Nature Phys.* **2008**, *4*, 213–217.

32 Ando, T.; Nakanishi, T. *J. Phys. Soc. Jap.* **1998**, *67*, 1704–1713.

33 Ando, T.; Nakanishi, T.; Saito, R. *J. Phys. Soc. Jap.* **1998**, *67*, 2857–2862.

34 McEuen, P. L.; Bockrath, M.; Cobden, D. H.; Yoon, Y.-G.; Louie, S. G. *Phys. Rev. Lett.* **1999**, *83*, 5098–5101.

35 Gao, H.; Wang, L.; Zhao, J.; Ding, F.; Lu, J. *J. Phys. Chem. C* **2011**, *115*, 3236–3242.

36 Soler, J. M.; Artacho, E.; Gale, J. D.; Garcia, A.; Junquera, J.; Ordejón, P.; Sànchez-Portal, D. *J. Phys.: Condens. Matter* **2002**, *14*, 2745.

37 Kresse, G.; Furthmüller, J. *Phys. Rev. B* **1996**, *54*, 11169–11186.

38 Perdew, J. P.; Burke, K.; Ernzerhof, M. *Phys. Rev. Lett.* **1996**, *77*, 3865–3868.